Active image optimization for lattice light sheet microscopy in thick samples

MAXIME MALIVERT,[1,2] **FABRICE HARMS,**[2] **CYNTHIA VEILLY,**[2] **JEROME LEGRAND,**[2] **ZIQIANG LI,**[3] **EMMANUELLE BAYER,**[3] **DANIEL CHOQUET,**[1,4] **AND MATHIEU DUCROS**[1,*] (iD)

[1]*Université de Bordeaux, CNRS, INSERM, Bordeaux Imaging Center (BIC), UAR 3420, US 4, F-33000 Bordeaux, France*
[2]*Imagine Optic, F-91400 Orsay, France*
[3]*Université de Bordeaux, CNRS, Laboratory of Membrane Biogenesis (LBM), UMR 5200, F-33140 Villenave d'Ornon, France*
[4]*Université de Bordeaux, CNRS, Interdisciplinary Institute for Neuroscience (IINS), UMR 5297, F-33000 Bordeaux, France*
[*]*mathieu.ducros@u-bordeaux.fr*

Abstract: Lattice light-sheet microscopy (LLSM) is a very efficient technique for high resolution 3D imaging of dynamic phenomena in living biological samples. However, LLSM imaging remains limited in depth due to optical aberrations caused by sample-based refractive index mismatch. Here, we propose a simple and low-cost active image optimization (AIO) method to recover high resolution imaging inside thick biological samples. AIO is based on (1) a light-sheet autofocus step (AF) followed by (2) an adaptive optics image-based optimization. We determine the optimum AIO parameters to provide a fast, precise and robust aberration correction on biological samples. Finally, we demonstrate the performances of our approach on sub-micrometric structures in brain slices and plant roots.

1. Introduction

For the last 20 years light-sheet fluorescence microscopy (LSFM) has become a very common and successful bio-imaging method [1]. More than 300 LSFM-based biology research papers were published in 2020. The reason of this success comes from a unique combination of three key imaging properties: (1) a very fast imaging rate, (2) an intrinsic optical sectioning and (3) a very low photo-toxicity and photo-bleaching [2]. LSFM is thus an ideal technique for fast, non-invasive, 3D imaging of live samples with high spatial resolution. LSFM implementations are very diverse with a wide range of commercial and home-made instruments, each addressing a specific range of sample size, imaging resolution, experimental conditions, or technical realization. In this growing forest of instruments, lattice light-sheet microscopy (LLSM) stands out as probably the most efficient microscope for gentle and fast 3D imaging at the sub-cellular scale [3]. The main difference between LLSM and other LSFM microscopes resides in the way the light sheet is created. In LLSM, the excitation laser beam is shaped by a spatial light modulator into an array of non-diffractive beams, also called an optical lattice. Restricting this optical lattice to the detection objective focal plane results in a very thin and uniform light sheet with a constant thickness over a distance much greater than the Rayleigh range of a focused Gaussian beam. Typical lattice light sheet thickness is ∼ 0.7 μm over 15 μm long along the propagation direction. This sub-micrometric homogenous optical sectioning plane provides LLSM superior imaging performances ideal to study 3D dynamics in biological samples at subcellular scales. Dissemination of LLSM technology was boosted by the group of E. Betzig at HHMI who shared the complete technical documentation to reproduce the original LLSM. Thus, many research groups and core facilities could access this powerful microscope. Soon after its initial publication,

LLSM was applied successfully to a number of biological research domains: quantification of membrane dynamics during cell division [4,5] study of transcription factors mechanisms [6], of organelles interaction [7], application to immunology researches [8,9], to oncology [10] or neuroscience. [11–14].

However, most of these studies were performed on very thin or semitransparent samples, or just below the surface of thick tissues. One of the main reasons is the presence of optical aberrations that alters light propagation from a straight path when imaging deeper inside a biological sample. The first cause of aberrations is the sample-media interface that represents, at the macroscopic level, an uneven surface with an index of refraction step. Furthermore, at the microscopic scale, any biological sample presents strong index of refraction inhomogeneities that modify the phase of light, inducing wavefront (WF) distortion [15,16]. As light penetrates deeper, typically beyond 100 μm, the WF is eventually randomized by successive scattering events. Here we address the sample-induced aberrations occurring at shallow depth before randomization of light phase. It is important to note that both excitation and detection paths of LLSM are affected by these sample-induced optical aberrations. Regarding the excitation path, the effects of the sample on the light sheet can be decomposed in two categories: (1) a deviation of the light sheet from its original position and (2) a broadening of the light sheet. In terms of deviation, the axial shift of the light sheet along the detection objective optical axis, also called defocus, is of critical importance as the light sheet thickness in LLSM is typically ∼ 0.7 μm and the detection objective depth of field ∼ 0.7 μm. Failing to achieve a perfect overlap between the light sheet and the objective focal plane results in reduced signal and resolution. In the present work we propose a method to automatically find the light sheet axial position that creates the best focused image. Illumination path aberrations other than defocus might also affect the light sheet position and shape but are not compensated by our approach.

Regarding the detection path, the aberrations also degrade the imaging PSF and result in a lower resolution and intensity. The effects of optical aberrations on image quality can be reduced or cancelled with adaptive optics (AO) strategies [17,18]. AO consists in correcting the aberrations with a WF shaping device such a deformable mirror (DM) or a spatial light modulator (SLM). Two classes of AO methods exist: direct or indirect [18,19].

In direct AO, the aberrated WF is measured with a WF sensor and the opposite WF is applied to the DM or SLM. The WF can be measured from a point source within the sample, for example a fiduciary fluorescent bead [20]. However, this strategy is difficult to implement within biological specimen. A less invasive solution consists in creating an artificial guide star using 2-photon excitation of sample fluorophores with a focused NIR femtosecond laser [21]. Also a more recent approach estimated the WF using an extended source WF sensor, that does not require either a real or artificial point source within the sample but uses a non-uniform contrasted feature within the sample itself [22,23].

In indirect AO, the WF is not measured, however, the aberrations can still be compensated using various strategies. If a point-like sub-resolution object can be imaged, one can acquire a PSF and estimate the local WF using the phase retrieval method [24]. Another more common method, named modal adaptive optics [25], consists in applying a series of controlled wavefronts shapes and measuring a metric on the acquired image for each WF. The set of WF that produces the highest metric determines the optimum aberration correction. The WF is typically decomposed in orthogonal modes such as Zernike polynomials and each mode is optimized separately. Various metrics (intensity [26–28], sharpness [29], spatial frequency content [30,31]) and optimization algorithms (model-based [32,33], hill climbing [34], genetic algorithm [35,36]) were developed [37]. Instead of applying changes to the entire WF, other teams use a zonal pupil method [38].

Correction of aberrations using AO has been used in many microscopy modalities among which LSFM is one. Adding AO capabilities to LSFM detection path significantly improved contrast inside multicell spheroids with direct AO method using in situ fiducials to measure WF

[39,40]. AO corrections at the excitation and detection paths of a LLSM was recently developed [41]. In this complex microscope the aberrated WF is measured successively at the excitation and detection paths using an artificial guide star produced at the focus of a NIR fs pulsed laser. The light sheet axial shift (defocus) is also corrected. Thanks to these corrections this AO-LLSM produced very high-quality images at depth that could not be reached by the conventional LLSM. For example, they demonstrated high resolution fast 3D imaging inside a zebrafish embryo. More recently AO-LLSM combined with big data analysis was applied to study clatherin-mediated endocytosis in organoids [42]. However, this AO-LLSM approach requires a complex integration and expensive instrument, with the addition of a NIR fs pulsed laser (to generate the guide star), the use of two full sets of AO systems (wavefront sensor and corrector), an upgrade of SLM in the excitation path, additional galvanometers, flip mirrors as well as several relay optics. Here we propose an alternative, simpler and low-cost two steps method: (1) light sheet defocus correction and (2) sensorless aberration correction at the detection path with AO. These processes allow to increase the resolution and contrast of images acquired with LLSM, especially in depth of the sample where the optical aberrations lead to the shifting of the illumination plane and the deterioration of image quality.

2. Methods

2.1. Optical system–alignment and calibration

Originally, our LLSM setup is a replica of the LLSM setup developed by Chen et al [3]. The excitation path (Fig. 1.a, blue) includes a Z galvanometer (GZ) optically conjugated to the back pupil of the excitation objective (EO, Special Optics, 28.6x 0.66 NA water). Rotation of GZ moves the light-sheet along the Z-axis, i.e., the optical axis of the detection objective (DO, Nikon 25x 1.1 NA water). The lattice pattern is created by the diffraction onto a programmable SLM and filtered by an annular mask. For all acquisitions in this work, we used a mask with inner and outer NA of 0.44 and 0.55 respectively. The resulting light-sheet had a quasi-uniform thickness over 15 µm length. Spatial resolution measured in the center of the field of view was 0.28 µm laterally and 0.55 µm axially. We modified the detection path (Fig. 1.a in green) to insert the AO capability and correct sample-induced aberrations. The back focal plane of the DO is imaged by a pair of achromatic doublet lenses (L1: f = 125 mm Thorlabs AC254-125-A, and L2: f = 101.6 mm Edmund Optics 49-783) in a 4f arrangement, folded using mirror M1, onto a fifty-two actuators DM (Imagine Optic - MirAO 52-e). The magnification (0.81) of this pair of lenses ensures that the full objective back aperture (D = 17.6 mm) is imaged at the DM pupil (D = 15 mm) without loss. A third lens (L3: f = 400 mm, Thorlabs; AC254-400-A) forms an image of the sample on the sCMOS camera with a 62.5× magnification. The entire optical path was designed using OpticStudio (Zemax) in order to minimize instrumental aberrations. A deviation path, composed of a flip mirror (FM), a fold mirror (M3) and an achromatic doublet lens (L4: f = 75 mm, Thorlabs AC254-75-A), allows to conjugate the back focal plane of the detection objective onto a Shack-Hartmann wavefront sensor (WFS) (*Imagine Optic – HASO 4 First*). This AO hardware integration requires to follow a precise alignment protocol detailed in Supplementary Note 1. WFS is used for two reasons: (1) to calibrate the DM, i.e., compute the interaction matrix between the DM 52 actuators positions and the WF shape ("*DM calibration*" Fig. 1(b), Supplementary Note 2 for details) and (2) to cancel static instrumental optical aberrations ("*Static aberration corrections*", Fig. 1(b), Supplementary Note 3). For this step 1 µm diameter fluorescent beads (Thermofisher Yellow-Green F8823) (Supplementary Note 6.1.) are illuminated and a closed loop AO process is applied, using fluorescent light from a single bead, between the DM and the WFS to correct static instrumental aberrations and obtain a flat WF after the DM. We consider, following the Maréchal criterion, that the calibration is correct when the residual WF is smaller than 35 nm RMS for an imaging wavelength of 488 nm. The previous compensation of static aberrations might be inaccurate in the case of significant non-common path aberrations. In our setup, such

aberrations can mainly be due to poor flatness of the flip mirror (Thorlabs BB1-E02). The flatness specification of this mirror being λ/10 (633 nm) we consider non-common path aberrations to be negligible in our setup. The WF shape calculated during this process corresponds to the initial shape used before each sample WF optimization. Static aberrations might change during the experiments due to minor temperature variation or opto-mechanical elements instability, but such variations will be taken into account when performing AO on the sample. During the rest of our optimization method the WFS is not used, as since our approach is image-based.
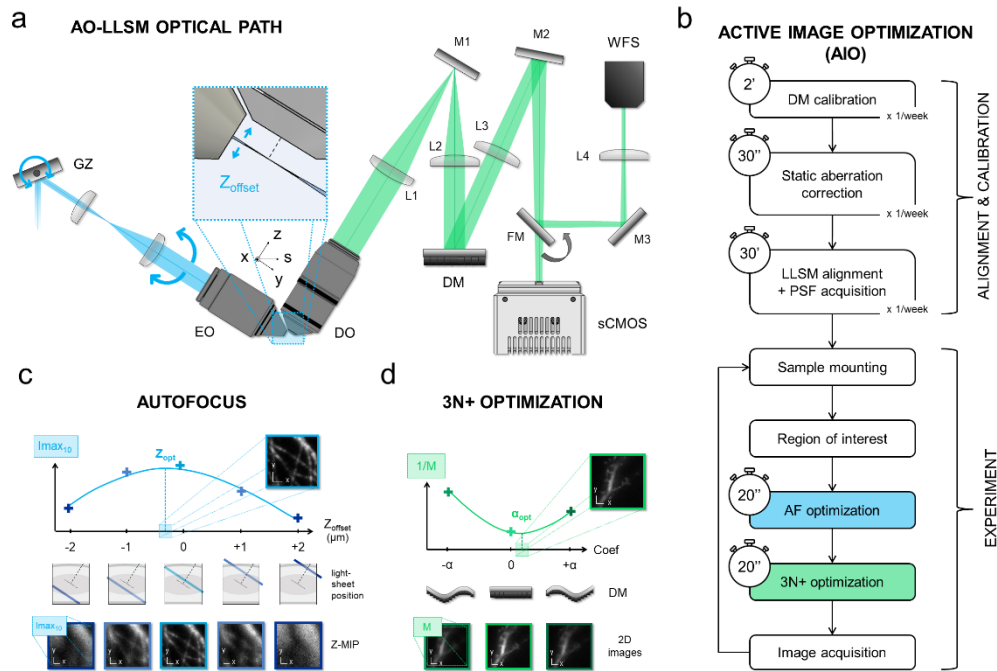

Fig. 1. Active image optimization (AIO) is based on automatic light sheet refocusing and detection path aberrations correction **(a)** Simplified optical diagram of the AO lattice light-sheet microscope. In the illumination path (blue) GZ galvanometer controls the light sheet position along the Z-axis (Z_{offset}). In the detection path (green) the deformable mirror (DM) modifies the WF to correct the optical aberrations using a sensorless iterative optimization process. **(b)** AIO steps, their frequencies and duration. **(c)** Principle of the "Autofocus" process: a minimum of five 3D stacks (30 images, 0.345 μm steps) are acquired, each with a specific Z_{offset} (e.g.-2, -1, 0, +1 and +2 μm). The maximum intensity projections (Z-MIP) along the Z axis of the 3D acquisition are measured for each stack (b, bottom) and the Z-MIP signal intensity is computed ($Imax_{10}$: mean of 10 brightest pixels). Finally, the Z_{offset} that maximizes $Imax_{10}$ (Z_{opt}) is interpolated and applied to GZ. **(d)** Detection path aberration correction using an image metric (3N+). A set of negative, null and positive coefficients (α) is applied on a given Zernike mode by setting the WF with the DM. A metric M is measured on the 3 corresponding 2D images and a 2nd order parabolic curve is fit to 1/M. The apex of this curve provides the coefficient α_{opt} that optimizes the image metric for the specific aberration mode. In case α_{opt} is not reached in the range [-α, +α], additional α points are measured (see text below). We repeat this process for all selected Zernike modes.

Once the detection path static aberrations have been canceled, the light sheet is co-aligned with the detection objective focal plane (manual tip/tilt, and translation adjustments of the LLSM) and a PSF is acquired on a 170 nm diameter bead (Fig. 1.b, "*LLSM alignment + PSF acquisition*", Supplementary Note 4 – beads sample protocol in Supplementary 6.1.). These

alignment and calibration procedures should be performed every time the sample immersion medium or temperature are modified. When keeping the same experimental conditions, we empirically determined that it was necessary and sufficient to repeat these steps once a week.

2.2. Active image optimization (AIO) process

Our AIO process consists in (1) a light sheet autofocus correction (AF, Fig. 1(c)) followed by (2) a detection path aberration correction (3N+, Fig. 1(d)). Typically, full AIO takes 40 s, with ~ 30 s actual sample exposure time. Here we describe the general principle of these two steps, integrated in a LabVIEW stand-alone software (Supplementary Note 5). We conducted benchmark tests to determine the AF and 3N+ parameters that provide the fastest and most robust performances, and that are presented further in the Results and Supplementary sections.

2.2.1.   Autofocus (AF) correction process

Once the sample is mounted and a ROI is selected ("*Sample mounting*" and "*Region of Interest*" (ROI) in Fig. 1(b)), the first step of our AIO consists in correcting the defocus between the illumination plane and the focal plane of the detection objective ("*AF optimization*" in Fig. 1(b)). We base this process on the maximization of a metric computed from the images acquired by the sCMOS camera. Our metric $Imax_{10}$ is the sum of the 10 brightest pixels measured on maximum intensity projection (MIP) of a 10 μm thick Z-stack (Z-MIP images in Fig. 1.c). Specifically, we acquire multiple Z stacks (30 planes, 0.345 μm steps) with a different light-sheet Z_{offset} (gradient blue lines in Fig. 1.c) between -2 and +2 μm. We chose this range because we observed that defocus remains within these bounds in all our experimental conditions. In Fig. 1.c the case with five images acquired with Z_{offset} at -2, -1, 0, +1 and +2 μm is presented. When the illumination plane is shifted away from the focal plane, the excitation and detection PSF do not overlap axially and the resulting PSF peak is reduced. Hence the image signal is reduced and the metric $Imax_{10}$ decreases. On the other hand, $Imax_{10}$ is maximum when the illumination plane and the focal plane perfectly overlap. We compute $Imax_{10}$ in a MIP of a 10 μm thick 3D stack instead of a single 2D image (~ 0.5 μm thick) to increase the sample information content over which we optimize the best focus. The offset that maximizes $Imax_{10}$ is interpolated with either a gaussian or parabolic function (Z_{opt} in Fig. 1.c). Finally, Z_{opt} is applied to GZ to refocus the light sheet.

2.2.2.   3N+ aberration correction process

In this step we correct the aberrations represented by Zernike polynomials [43], which are continuous and orthogonal functions used to describe aberrations in optical systems. The Zernike aberration decomposition is very commonly used because there is almost no cross talk between these polynomial functions (aka modes). The wavefront deformation, measured as the root mean square (RMS) deviation from a flat wavefront, increases with the amplitude of each Zernike polynomial. We correct Zernike modes sequentially, typically starting with astigmatism ("*3N+ optimization*" in Fig. 1(b)). The sample aberrations arise from refractive index mismatch between the imaging solution and the sample and from sample inhomogeneities. Aberrations tend to increase with the imaging depth. In a similar way as AF, the goal is to optimize an image-based merit factor. We use an iterative process sequentially on each Zernike mode. Thanks to the previous DM calibration, the DM is capable to accurately apply a pre-defined WF shape based on a Zernike representation. The correction process consists in applying a positive, null (initial mirror shape) and negative coefficient to a specific Zernike mode (+α, 0 and -α in Fig. 1(d)) and to measure the corresponding image-based merit factor. In our case the merit factor is the inverse of a metric, such as e.g., the maximum intensity or the energy from a pre-defined spatial frequency domain (see benchmarking section below). We fit the measured data points with a second order polynomial to interpolate the coefficient (α_{opt} in Fig. 1(d)) that maximizes the merit

factor for the selected Zernike mode. This coefficient cancels out most of the corresponding Zernike aberration from the detection WF and consequently, increases signal and resolution.

Our aberration correction process is designed to speed up optimization without sacrificing precision. It presents two improvements when compared to most common AO algorithms [25,32]. First, in order to simplify processing, we use a parabola to fit the 1/M merit factor and find its minimum. This is a very fast and direct algebraic calculation. Other 3N algorithms [32] are often based on a slightly more complex Gaussian fit of M. The second improvement consists in a simple logical method to measure 1/M in a minimum but sufficient number of points. Since sensorless optimization is blind to the amount of aberrations to be corrected, an initial fixed value of α (see Fig. 1.d) has to be selected as a trade-off between precision (low α value = high sampling) and dynamic range (large α value). In order to minimize the number of images required from the iterative procedure (and minimize optimization time and photobleaching), usually only three images per Zernike modes (3N or 2N+1 algorithm) are used. Here we start with three measurements for coefficients $-\alpha$, 0 and $+\alpha$. If the parabola minimum is within this range, then the optimization process is terminated. If not, we measure the merit factor at either $+2\alpha$ or -2α depending on the parabola slope and a new parabola fit is computed with added points (e.g., $-\alpha$, 0 $+\alpha$ and $+2\alpha$). In the event that the minimum is still not reached and if the number of iterations is below a predefined limit, another iteration is launched. If not, or if an iteration converges to wrong calculation, none coefficient is applied and the algorithm switches to the next Zernike mode. As a result, our optimization process uses three images in ideal cases – i.e., when the Zernike aberration coefficient is in the search range -, and only a couple of supplementary acquisitions, when necessary, thus minimizing the total number of images. We named this adaptive sensorless aberration correction method 3N+. The complete organization chart of the algorithm is available in Supplementary Fig. S1.

3.   Results

As described in the Introduction, a wide variety of approaches exist for AF corrections and 3N optimization in microscopy and vary in their calculation method, input parameters, system integration and performances. Overall, optimizing the performance of AF and 3N processes requires to tailor their parameters, in particular considering the specificities of the samples of interest, the signal to noise, the amplitude of aberrations to be compensated, or the expected accuracy of the correction. With the aim to both maximize the quality of the correction and minimize the time required for both processes, we conducted a systematic analysis of the impact of the key parameters of the AF and 3N+ processes, including for the AF process the number of offset points, and for the 3N+ process the comparison of several merit factors, the amplitude of the sampling step and order of modes of the modal process, and the overall number of iterations.

All images processing and acquisition conditions presented in the following section and in supplementary are defined in Supplementary Note 7 and 8.

3.1.   AF process optimization

First, we tested the AF process by imaging COS cells with three types of labeled structures (Supplementary Note 6.3.): a quasi-homogeneous labeling of cell membranes (Fig. 2.a, membrane, blue), filamentary structures (Fig. 2.b, tubulin, green) and punctate, high spatial frequency signal (Fig. 2.c, clathrin, red) in order to assess the reliability of AF when applied to different sample types, corresponding for example to different spatial frequencies. To optimize both precision and speed we tested our AF process with either five or nine Z_{offset} data points. Sampling the defocus with nine points could potentially provide higher precision. On the other hand, sampling only five points would be faster and reduce photobleaching. We also tested fitting the data with either a gaussian or parabolic curve. We expected the $Imax_{10}$ metric to decrease symmetrically for small (+/- 1 µm) positive or negative defocus (reduced PSF peak). However, the shape of $Imax_{10}$

for larger defocus is not straightforward and most likely sample dependent. We decided to test empirically both curves in various samples to determine the best fit (results for the parabolic curve fit in Supplementary Fig. S2). First, we achieved a perfectly focused light sheet by using "Autofocus Bead" function of LLSM software (Supplementary Note 4) on one of 170 nm diameter beads included in the COS cell cover slip with poly-L-lysine. Then we applied four defocus (-1 µm / -0.5 µm / +0.5 µm / +1 µm, "applied offset" Fig. 2(d)) by tilting the Z-galvo (GZ) and launched the AF process to measure the defocus ("measured offset" Fig. 2(d)).

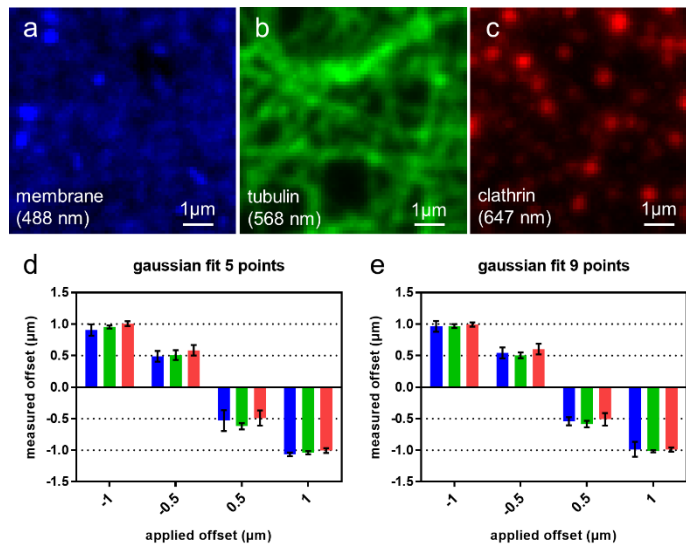**Fig. 2.** AF process is precise and reliable. We test AF on three cellular structures imaged in a $6 \times 6\ \mu m^2$ ROI in COS cells: (a) membranes (WGA conjugated to Alexa 488 nm), (b) tubulin (immunolabelling with Alexa 568) and (c) clathrin (immunolabeling with Alexa 647). Four defocus are applied: -1 µm, -0.5 µm, +0.5 µm and +1 µm. AF processes based on (d) 5 points or (e) 9 points fit with a Gaussian curve are launched to correct this applied defocus. In both cases and for each labeling, the averaged measured defocus on five FOVs allows an accurate correction.

Here, we present the variation of the average measured offset on five FOVs for three colors with the applied initial offset for the gaussian fit on five points (Fig. 2.d) and on nine points (Fig. 2.e). The results for the AF process based on a 2nd order polynomial fit are presented in supplementary (Supplementary Fig. S2). We show that the AF process based on a gaussian fit allows to recover the position of the light-sheet on the focal plane of the detection objective with five or nine measurements with a good repeatability and reproducibility. The average defocus measured have a low error and standard deviation (relative to the defocus amplitude) with any type of sample and applied offset. The maximum mean square deviation between the measured and applied defocus values is measured on the gaussian 5 points AF on membrane labelling, with a value of 0.11 µm. For the other fits applied to the three labeling, this value is below 0.09 µm, which demonstrates the effectiveness of the method in correcting the defocus with few errors. Thereafter, we will use the AF process based on a gaussian fit and five measurements to decrease the processing time and reduce the risk of photobleaching.

3.2. Comparison of several merit factors for 3N+ process

Regarding the 3N+ process, the optimal parameters of the algorithm are dependent on the characteristics of the image. In particular the merit factor is strongly influenced by the sample

intensity, SNR, and spatial frequency content. We compared three metrics: the maximum intensity averaged on 10 brightest pixels ($Imax_{10}$ –left image in Fig. 3.a), the signal integrated in a Fourier ring for spatial frequencies either in the range 500-1000 mm^{-1} ($FFT_{500-1000}$ – centered image in Fig. 3.a) or 1000-2000mm^{-1} ($FFT_{1000-2000}$ – right image in Fig. 3.a). The microscope theoretical cutoff frequency is $\sim 3600\,mm^{-1}$ (NA = 1.1, λ=500 nm), in good agreement with the measured lateral resolution of 275 nm. We selected frequency metrics below this cutoff frequency to remain in a range where the signal is significantly above the noise level and the AO process gain can be clearly detected. Furthermore, the specific neuronal sample imaged here presented bright structures such as spines and dendritic branches, with sizes between 2 μm - 1 μm ($FFT_{500-1000}$) and 1 μm - 500 nm ($FFT_{1000-2000}$). The corresponding merit factors are the inverse of these metrics. We tested the merit factors sensitivities on dendrites labeled with cytosolic GFP in a fixed mouse brain slice (e.g., Fig. 3.a left, Supplementary Note 3). Five ROIs were selected at the surface of the brain slice. At each ROIs we applied varying amplitudes of aberration coefficients (-0.15 till +0.15 μm RMS, 0.05 μm steps) for Zernike modes from astigmatism 0° to trefoil 90° thanks to the calibrated DM that can induce a precise quantity of any Zernike aberration. For each coefficient, one image is acquired and the three merit factors are measured. The results for the effect of spherical aberration are presented on Fig. 3.a, bottom. Data for all other aberration modes are presented in Supplementary Fig. S3.
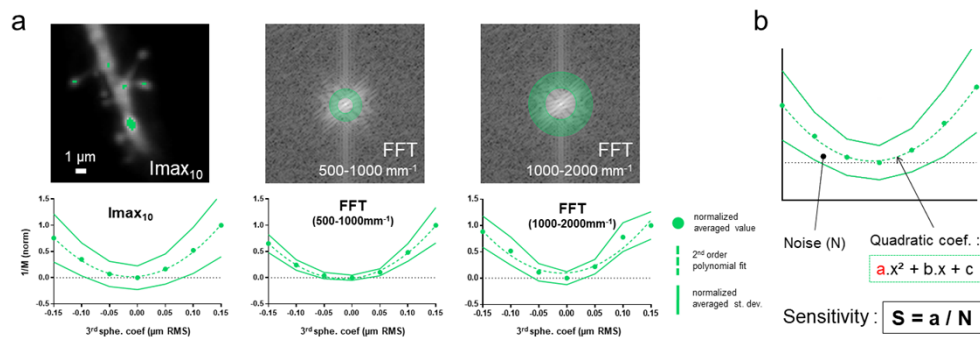

Fig. 3. Comparison of three merit factors for the 3N+ process. **(a) top**: Illustration of the pixels used to compute the merit factors, either on the LLSM image of a neuronal dendrite ($Imax_{10}$ – more than 10 pixels for illustration), or on the 2D Fourier transform ($FFT_{500-1000}\,mm^{-1}$ and $FFT_{1000-2000}mm^{-1}$); **bottom**: Normalized response of the three merit factors as a function of applied spherical aberration coefficient between -0.15 and 0,15 μm RMS, measured on neuronal dendrites expressing GFP. The merit factors (green dot) are measured and averaged on five different areas in the sample, green line indicating the standard deviation edges. Data are fitted with a second order polynomial curve (dashed green line). **(b)** For each response curves we measure a sensitivity factor defined as the ratio of the parabola quadratic coefficient divided by the noise N.

We then asked ourselves which merit factor gives the greatest chance of our 3N+ algorithm to converge with a minimum number of steps and the smallest error. For this we computed a sensitivity factor defined as the quadratic coefficient of the polynomial fit ("a" in Fig. 3(b)) divided by the integral of the noise N (grey area in Fig. 3(b)). A large S means that a small aberration will induce a large merit factor change with low noise, thus increasing the probability of our 3N+ algorithm to converge fast and precisely to the global minimum. These sensitivity factors are presented in Table 1.

$Imax_{10}$ systematically results in lower sensitivities than the two FFT metrics. $FFT_{500-1000}$, which integrates image information in the spatial frequency range corresponding to fine dendrites and spines – i.e., structures most impacted by aberrations - gives the best result for all modes

Table 1. Sensitivity factors for most relevant Zernike modes for neuronal samples investigated[a]

Metric Zernike mode	Dendrites in brain slice (GFP)		
	Imax_{10}	$\text{FFT}_{500-1000}$	$\text{FFT}_{1000-2000}$
Astig 0°	50.6	190.4	**228.6**
Astig 45°	70.2	243.8	**260.6**
Coma 0°	108.6	**339.6**	286.9
Coma 90°	115.2	**418.7**	273.9
3rd spherical	188.4	**532.2**	322.8
Trefoil 0°	82.5	**335.5**	240.6
Trefoil 90°	83.4	**325.6**	220.7

[a]Average values are calculated on five FOV for each sample. Highest values for each Zernike modes are show in bold.

except astigmatism where $\text{FFT}_{1000-2000}$ provided a very small increase in sensitivity. Overall, we conclude that the $\text{FFT}_{500-1000}$ provides a sensitive metric for this type of sample and we selected it as the merit factor for all the subsequent tests and experiments with the 3N+ process.

3.3. Optimization of other 3N+ parameters

In addition to the merit factor, other input parameters impact the 3N+ algorithm accuracy and must be carefully selected to precisely correct sample induced optical aberrations. (1) The Zernike mode search range α defines the sampling step to find the optimum Zernike coefficient and so is directly related to the 3N+ result accuracy. (2) Zernike mode correction order is critical because correcting first the mode that degrades the most the image can increase the sensitivity for the following modes. (3) The number of iterations n of the 3N+ algorithm can increase progressively the accuracy of the process (at the cost of slowing down the AO process)

We tested the effects of the range α, the Zernike mode orders and the iteration number *n* on fixed brain slices with labeled neurons (Supplementary Note 3). First, we start from a reference mirror shape corresponding to a flat WF, i.e., the imaging path corrected from static aberrations, and imaged a fine dendritic structure at the surface of the sample ("*ROI at surface*" in Fig. 4(a)). Then, to mimic the effect of light propagation inside the sample, we induced an artificial aberration by generating a random set of Zernike coefficients between 0 and 200 nm RMS and from astigmatism 0° to trefoil 90° ("*DM$_\Delta$*" in Fig. 4(a)). The aberration is applied by changing the shape of the DM. Acquisition parameters are chosen to avoid photobleaching during the 3N+ process experiment (Supplementary Note 8). After an AF, to correct potential light-sheet defocus, we ran three successive iterations of the 3N+ process that output three sets of Zernike coefficients (green inset in Fig. 4.a) and correspond to three mirror shapes. This experiment is reproduced ten times in ten different selected areas at the sample surface, to integrate 100 measurements for significant statistical analysis.

In Fig. 4, we present the results of a 3N+ process where we chose to correct aberrations in the following order: 3rd spherical, astigmatism 0°, astigmatism 45°, coma 0°, coma 90°, trefoil 0° and trefoil 90°. This 3N+ optimization is repeated three times, with iterations 1, 2, and 3 having α amplitudes 100, 50 and 50 nm RMS respectively. Mismatch between sample and immersion medium refractive index lead to spherical aberrations in depth. By correcting it first, we intend to suppress a significant part of WF deformation and improve correction on subsequent modes. We set the first iteration amplitude to 100 nm RMS as this is a representative value of the typical aberrations we observed in our samples in depth, and represents a good compromise between
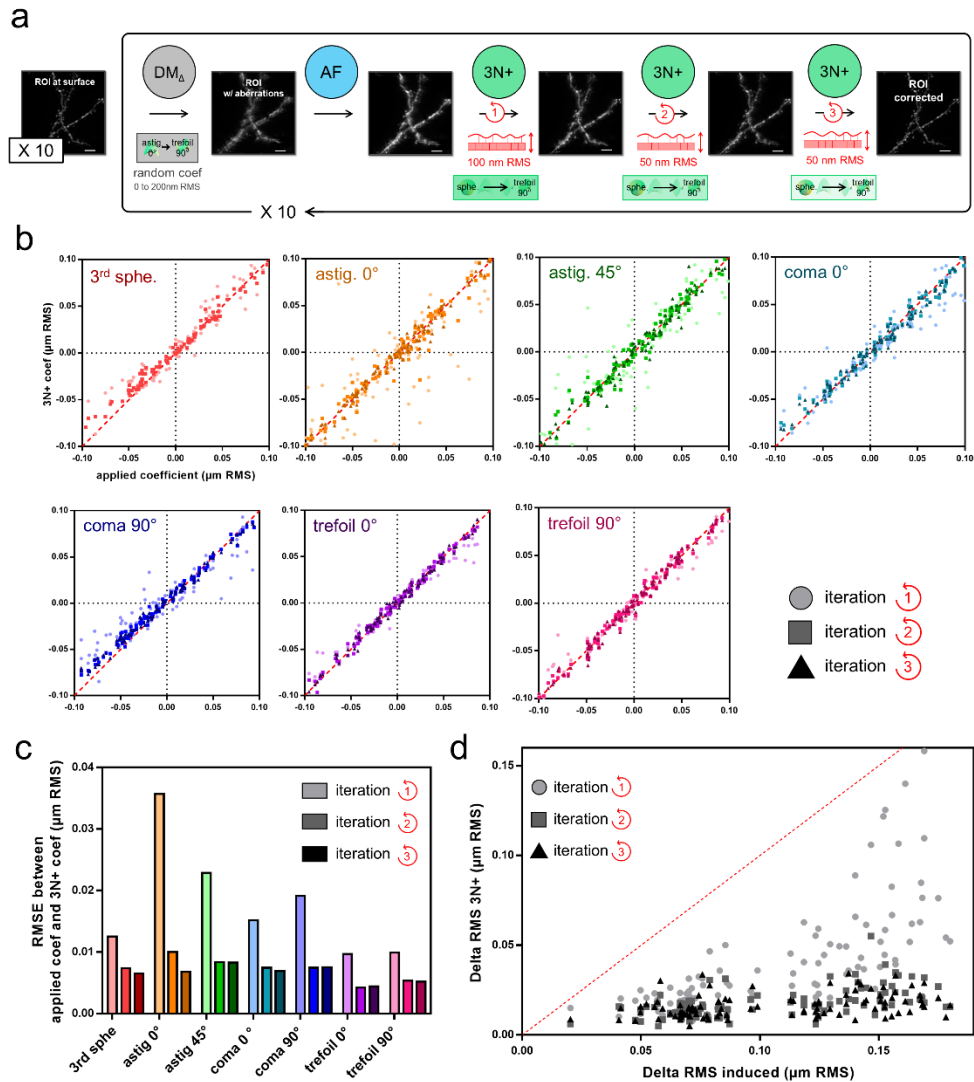
Fig. 4. The 3N+ process efficiently corrected artificially-induced aberrations. (a) We acquired a non-aberrated image at the surface of a brain slice with labeled dendrites, then added a random set of aberrations from astigmatism to trefoil (random coef. in grey) with the DM (DM_Δ) and run three iterations of the 3N+ process (green circles) after an AF (blue circle). For all iterations, 3rd spherical aberration is corrected first. For iteration 1, DM had an amplitude of 100 nm RMS, and then 50 nm RMS was applied for iterations 2 and 3. The same process was repeated 10 times on 10 different areas of the sample with a different randomly generated aberration. (b) 3N+ coefficient found after each iteration as a function of applied coefficient on DM, for each Zernike mode. Red dashed line corresponds to a perfect 3N+ correction. An excellent correlation between applied and measured coefficients is showed for all Zernike modes. (c) Root mean square error (RMSE) are extracted to show the 3N+ error for each Zernike mode at each iteration. (d) We computed the induced and residual WF $\Delta RMS_{induced}$ and ΔRMS_{3N+} respectively using the known DM shapes and calibration matrix. After only 2 iterations the residual WF is 50 nm RMS, independently of the induced aberration

measurement speed and accuracy. The next two iterations allow to refine the algorithm precision. Two other 3N+ process with different orders of optimization and amplitudes are described in Supplementary Fig. S4. The 3N+ process presented in Fig. 4 provided the best results in terms of correction speed and accuracy.

We can plot the 3N+ process output coefficients vs. induced coefficients for each Zernike mode (Fig. 4.b). We see that 3N+ is very efficient, especially after 2 iterations, since most points fall on the identity line. For each iteration and each Zernike mode, we can estimate the accuracy of the 3N+ process by computing the root mean square error (RMSE) of the coefficients found with the 3N+ vs. induced coefficients (Fig. 4.c). After the second iteration, all induced aberrations are corrected with an error lower than 10 nm RMS. We notice that an error superior to 20 nm RMS on astigmatism is still present after the first iteration, independently of the Zernike order used for the correction (Supplementary Fig. S4), demonstrating the lower efficiency of 3N+ on astigmatism. This particular behavior of the process on astigmatism might be attributed to some drift of the DM shape with temperature, membrane DMs being known to be sensitive to temperature variations in particular regarding astigmatism at first. The latest version of the DM used includes a stabilization module (Imagine Optic MirAO52ES - https://www.imagine-optic.com/products/mirao-52es-deformable-mirror/), which is planned to be integrated in our setup to mitigate this possible effect.

The corrected WF could then be computed and the residual aberration expressed as the WF ΔRMS computed and plotted as a function of the induced WF ΔRMS (Fig. 4.d). Contrary to the measurement for each individual Zernike mode, this representation provides a global estimate of the performance of the 3N+ process. Independently of the quantity of aberrations induced (at least up to 200 nm RMS), the 3N+ algorithm is capable to correct the aberrations to less than 50 nm ΔRMS after only two iterations for 99/100 test points. A 3rd iteration does not result in a significant supplementary gain.

This 3N+ process - spherical aberrations corrected first, and two 3N+ iterations are run with respectively 100 nm and 50 nm α amplitudes - obtained on images of neuronal dendrites offers the most accurate and efficient results compared to the other correction processes tested (see Supplementary Fig. S4). For all the results presented below, we used this 3N+ process along with the AF method and merit factor selected on Section 3.1 and 3.2.

3.4. Dendritic spines imaging in depth of a brain slice

After optimizing the parameters of AF and 3N+, we tested the complete process by imaging submicrometric structures in fixed organotypic hippocampal brain slices in depth (Supplementary Note 3). Specifically, we imaged the width of dendritic spine heads in neurons expressing cytosolic GFP at approximately 40 μm depth, where the imaging quality is typically significantly degraded compared to the surface. First, the light-sheet position and the mirror shape were optimized on dendrites at the surface to correct system aberrations. Then, dendritic spines were imaged between 38 and 44 μm under this surface in three steps: (1) before any type of correction, (2) after AF optimization and (3) after 3N+ optimization process. To quantify the impact of these optimizations, the width of selected dendritic spine heads was measured at each of the three stages, by plotting an intensity profile perpendicularly to the spine necks (Fig. 5(a)) and by measuring the full width at half maximum (FWHM) of the profile gaussian fit. A total of 67 spines were examined for the three optimization steps, taken from 8 different experiments – all issued from the same sample preparation – and were included in the ANOVA test which results are displayed in Fig. 5(b).

Without correction, the average spine head width measured on dendritic spines increased to 0.493 μm ± 0.100 μm compared to the average size at the surface equal to 0.397 μm ± 0.062 μm (n = 134, dot dashed line in Fig. 5.b). After AF, this value is strongly reduced at 0.424 μm ± 0.080 μm. After 3N+ spines almost recover their size at the surface (0.400 μm ± 0.079 μm). ANOVA
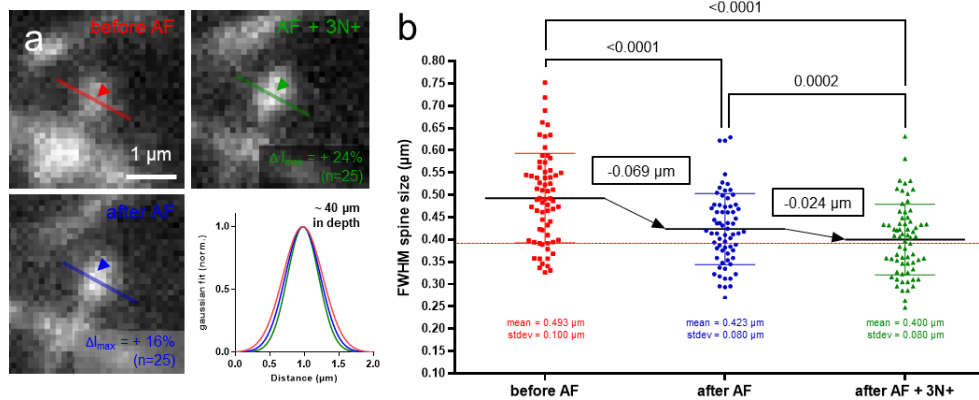
Fig. 5. The active image optimization (AIO = AF & 3N+) process recovers an accurate morphological representation of dendritic spines down to 40 μm below brain slice surface. (a) Spine head widths are measured before AIO (red), after AF optimization (blue) and after AIO (green). We define the spine head width as the FWHM from a gaussian fit of intensity profiles perpendicular to the spine neck. We measured, at each step, the peak intensity profiles (black arrows) and found an intensity increase of +16% after AF and +24% after AIO (n = 25 spines). (b) ANOVA test on 67 FWHM measurements made on dendritic spines. For each set of data, averaged value and associated standard deviation are indicated as black horizontal lines and color error bars. AF decreases by 0.069 μm ± 0.011 μm on average, and 3N+ by 0.024 μm ± 0.005 μm. with ANOVA test respective significance threshold below 0.0001 and equal to 0.0002. After AIO, the average size of dendritic spines at the surface (red dashed line) is restored.

test also indicate significant difference of 0.069 μm ± 0.011 μm on average between the start and the AF (p < 0.0001), and 0.024 μm ± 0.005 μm between AF and 3N+ (p = 0.0002), and 0.093 μm ± 0.011 μm between the beginning of experiment and the last correction (p < 0.0001).

The results of this ANOVA test show a significant reduction of the dimension of this submicrometric neuronal structure thanks to the resolution enhancement in depth provided by the AIO process. Both AF and 3N+ provide significant improvements although the correction power of 3N+ is less compared to AF, probably due to low aberrations quantity at this depth. Overall, we conclude that AIO greatly improves the accuracy of morphological representations of fine structures in depth of biological samples.

3.5. AOI and deconvolution process

Deconvolution is a post-treatment widely used in microscopy to decrease the noise and increase the resolution and contrast of acquired images. The principle of deconvolution is based on the fact that the acquired image is the convolution of the original sample 3D information by the PSF of the microscope. Any deconvolution algorithm requires an accurate PSF (or the Fourier domain OTF) that can be either computed from theoretical formulas or measured in situ. If the PSF is erroneous, the deconvolution result is necessarily artefactual. This is the case if an aberrated image is deconvolved with a PSF measured in a non-aberrating condition. In LLSM we typically measure the microscope PSF by imaging a small fluorescent bead on a cover slip surface. Deconvolution of images acquired in depth inside biological samples is likely to show poor quality if one uses the surface PSF. To enhance the deconvolution, a solution is to correct aberrations before the image acquisition.

The deconvolution on raw and aberration corrected images was tested on astrocytes expressing cytosolic GFP in a fixed organotypic mouse brain slice (Fig. 6.a., Supplementary Note 3 for

sample preparation) and living Arabidopsis root microtubules tagged to tagRFP (Fig. 6.b and 6.d, Supplementary Note 4). Although LLSM microscopy provides high-content information at the surface of the sample, it is impossible with conventional LLSM to observe structures in depth. As a result, biological studies on astrocytic fine processes and microtubules arrangement in Arabidopsis roots [44] are constrained to the surface. In order to show that it is possible to extend the LLSM imaging volume on these sample, we used our method on structures at ∼ 15 µm depth for these two samples.

Deconvolution is based on a Richardson-Lucy algorithm as described in the original LLSM article [3] (Supplementary Note 7).

Each step of our optimization process is illustrated with MIP of 30 planes (26.24×26.24 µm in XY) in Fig. 6(a) Astrocyte fine processes, not visible in raw image, appear thanks to contrast increase after the AIO on non-deconvolved data ("No AIO" and "AIO" images in Fig. 6(a)). After deconvolution, resolution is further enhanced, whereas some structures are not well resolved without AIO (comparison of "No AIO + deconv." and "AIO + deconv." images). It is particularly visible in zoom regions 1 and 2, where deconvolution induces artifacts of reconstruction without aberration correction. In region 1, astrocyte processes are separated after AIO ("AIO" and "AIO + deconv." of zoom 1 images) compared to blurred structures without AO ("No AIO" and "No AIO + deconv." of zoom 1 images). Structures from region 2 are divided in three filaments with AIO ("AIO" and "AIO + deconv." of zoom 2 images) where the two filaments at the bottom are confounded in background noise without optimization ("No AIO" and "No AIO + deconv." of zoom 2 images). AF and 3N+ allows to show more accurate structures even without deconvolution.

In Arabidopsis roots, microtubules create highly organized meshes at the cell periphery and have a role in cell division, expansion and morphogenesis. We illustrate this structure along two views: (1) a middle section of a cell where microtubules grow perpendicular to the image plane (Fig. 6(b)) and (2) a surface section of one cell where microtubule run parallel to the image plane (Fig. 6(d)). Without AIO correction, we hardly resolve any structures ("No AIO" in Fig. 6(b), 6(d) and grey dotted lines in top charts of Fig. 6(c) and 6(e)). Deconvolution alone does not allow to recover these filaments ("No AIO + deconv." Fig. 6(b) and Fig. 6(d)) and intensity peaks remain near the background noise (grey dashed lines in top chart of Fig. 6(c) and 6(e)). Thanks to AIO correction, we start observing filaments structures ("AIO" images from Fig. 6(b) and 6(d)) illustrated by high peak intensities compared to background (blue lines in top charts of Fig. 6(c) and 6(e)). Deconvolution enhances resolution, initiated by the AIO process with well resolved structures ("AIO + deconv." in Fig. 6(b) and 6(d)) and peak intensities increasing by ∼30% for microtubules filaments viewed perpendicularly compared to deconvolution without optimization (Fig. 6(c), bottom) and by ∼40% for parallel microtubules (Fig. 6(e) bottom).

We note that nuclei are also labelled in this Arabidopsis root sample (Fig. 6.b) because the plant express tubulin above the endogenous level. Not all tubulin could be incorporated into microtubule arrays and free tubulin would be seen in the cytosol and nuclear.

We also wanted to determine the relative gain due to AF alone Vs full AIO on deconvolved images (Supplementary Fig. S5). For the astrocyte sample presented in Fig. 6 the 3N+ step did not significantly improve the image quality, most likely because we are imaging at very shallow depth that does not induce significant optical aberrations. However, regarding the Arabidospis root, 3N+ clearly improves the image resolution compared to AF alone, as illustrated by the microtubule structures that are better defined. We believe that this sample induced stronger aberrations than brain slice due to its curved surface.
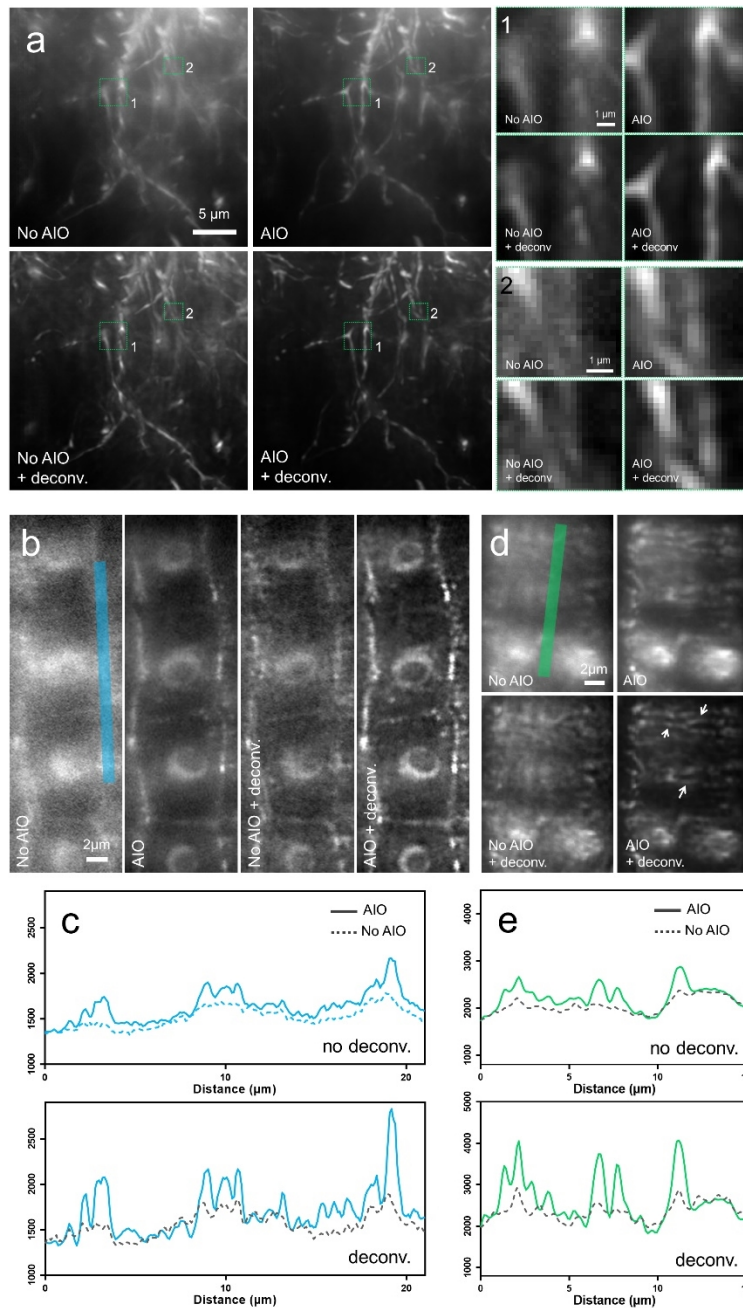
Fig. 6. Correction of aberrations with AIO before deconvolution provides significant artifact reduction as well as resolution and signal enhancement. (a) MIPs of 30 planes in an astrocyte expressing GFP at approximatively 15 μm in depth, in four conditions: raw data ("No AIO"), data after AIO ("AIO"), raw data deconvolved ("No AIO + deconv.") and AIO data deconvolved ("AIO + deconv."). Regions 1 and 2 are zoomed for each condition in right panel. (b) 2D slice in the center of Arabidopsis root cells around 15 μm in depth, with microtubules labeled with tagRFP, corresponding to the second layer after the epidermis. (c) Intensity profile (blue line in b.), in "no deconv." and "deconv." cases. AIO highlights microtubules which surrounded cells and enhances the deconvolution process. (d) MIPs on top of Arabidopsis root cell to image subcortical microtubules filaments around 15 μm in depth. Profiles along the cell (green line) show resolution increase in (e) on the corresponding intensity profiles. Deconvolution with AIO highlights microtubules filaments (white arrows in d).

4.   Discussion and conclusions

We developed an AIO process for LLSM that significantly improves image quality in depth in thick samples. Here a "thick" sample corresponds to any biological specimen for which the illumination or detection optical pathways are altered compared to a straight light propagation and that induce a noticeable reduction of image resolution and intensity. Our optimization process is based on merit factors from images acquired by the detection camera, and does not require to measure the WF emitted by a fluorescent point source within the sample. Our AIO is divided in two consecutive steps, AF and 3N+ that are both required. AF corrects the light-sheet position in less than 20 seconds and 3N+ strongly decreases the optical aberrations in another 20 seconds (2 iterations) from astigmatism to trefoil with a global residual WF error around 20 nm RMS (Fig. 4(d)). We apply first AF, then 3N+, the 3N+ process benefiting from the increase of signal brought by the AF process. Indeed, it has been recently demonstrated in an adaptive LSFM setup that the sequence of optimizing the illumination followed by correcting aberrations of the detection path provides an optimal image enhancement, as compared to the opposite sequence [45]. Despite this method takes more time than direct WF correction [19,18], it avoids the use source points – beads or artificial guide stars - and a deviation path for a WFS. Thus, the sample preparation is facilitated (no fiducials required), and the system is more light-efficient. Additionally, the cost and complexity of our approach is reduced compared to other aberration correction systems that require an expensive NIR fs pulsed laser to generate an artificial guide star and a WFS. Our method is applicable to any LLSM, but could be easily adapted to other LSFM detection path at a reasonable cost.

In this work, we have tested low level merit factors for the 3N+: intensity and Fourier domain ring integration. However, complex merit factors in terms of filtering process or spectral content probed, might further increase the 3N+ efficacy, especially on samples with a different spectral content as compared to the dendrites presented in Fig. 3 and 4. An example could be one of the spectral image quality metrics defined by Royer et al. [46] and, in particular, the normalized Discrete Cosine Transform Shannon entropy (DCTS). Indeed, DCTS was identified as the optimum image quality metric for light-sheet microscopy with excellent separation of signal and noise to reveal the useful content of the image.

It should be noted that we did not study the effect of the image SNR on the convergence of the AIO process. Our results are obtained with typical signals of 350 photons/pixels integrated over 300-1000 pixels/image. A future study is required to determine the minimum SNR to reach satisfactory aberration correction based on our AIO method. As a first order of magnitude, [26] showed that typically 2000 photons per mode and per iteration are sufficient to reach a Strehl ratio above 0.9. Even if we do not expect a significantly different result regarding the 3N+ process, it could be interesting to study the minimum SNR required for accurate AF. Likely, we should determine a compromise between SNR, efficient correction, convergence speed and photobleaching.

Also, we decided to correct only the axial defocus of the light-sheet in the excitation path. Royer et al. [46,47] developed a very thorough automatic procedure based on the SIMView microscope to compensate any axial, lateral or angular mismatch between light-sheet and detection focal plane. This light sheet re-alignment is performed automatically thanks to several motorized opto-mechanical devices. However, in the case of LLSM, Liu et al. showed that, in most samples, the light sheet pitch angle generates a negligible defocus within the small LLSM FOV (see [41] Supplementary Fig. S3.). Therefore, we decided to implement a basic axial light sheet refocusing method and our results show that, in our experimental conditions, this simple AF approach is sufficient to significantly improve image quality (see "before AF" and "After AF" in Fig. 5(b)). Furthermore, our approach does not compensate for optical aberrations in the illumination path other than axial defocus. It could be achieved for example by adjusting the WF with a SLM

in the light sheet path as in [41]. This option would likely provide even higher image quality improvement in depth.

We have also observed that the image resolution and contrast is greatly improved by the AF, whereas the additional gain provided by the 3N+ process is often comparatively smaller. This is likely due to the fact that the samples were imaged at shallow depth, where optical aberrations are small and mostly created by the minor mismatch between the sample and immersion medium indices of refractions. Still, the resolution improvement provided by the 3N+ process is illustrated by the spine head size reduction (Fig. 5(b), "After AF + 3N+") and in the image of the Arabidospis root presented in Fig S5. Further studies on more aberrating samples such as zebrafish embryo could help to better determine the relative gain of AF and 3N+ steps.

Even if our AO detection path method offers several advantages, the aberration correction is not optimal when compared to closed-loop correction [41]. The integration of extended source WFS [22,23] and double labelling in our method could be a relevant next step to improve the performance of AO correction, still avoiding the requirement of a point source in the sample, and minimizing photon loss for structures of interest.

We optimized AF and 3N+ parameters and demonstrated that the loss of spatial resolution when imaging in depth in thick samples can be almost canceled by AIO, as illustrated by the measurement of dendritic spine head widths at 40 μm (Fig. 5). Further studies are required to determine the maximum depth up to which AIO provides a significant resolution improvement. This value is clearly sample dependent and is ultimately limited by light scattering. Extending the imaging depth for LLSM in thick samples is critical for many biological studies. For example, in acute brain slices, which are a very common integrated model for neuroscientists, the cells at the surface are damaged during the sectioning process. Hence it is essential to study cells at depth greater than 20 μm. This is now possible thanks to the high-resolution imaging provided by the combination of LLSM and our AIO process.

We also showed that the accuracy of the 3D deconvolution of LLSM data is strongly affected by sample aberrations (Fig. 6). Without AIO the deconvolution results seem to be improved compared to before deconvolution, but are actually prone to artifacts. On the other hand, AIO followed by deconvolution allows to observe fine submicrometric details inside brain slices or Arabidopsis roots. Deconvolution is a critical step for 3D structural imaging it is thus essential that the deconvolution process can be trusted. Our approach could also be used for SMLM. The combination of LLSM and SMLM has been demonstrated by [48]. Any loss of resolution due to aberrations would reduce the number and localization precision of single molecules. As demonstrated by [31], AO strategies can significantly improve the output of SMLM algorithms. Furthermore, AO can be used to increase the Z localization precision in super resolution by adding a controlled amount of astigmatism [49]. Therefore, the combination of LLSM and AO opens the way for efficient 3D super resolution microscopy inside thick samples.

Data availability. Data underlying the results presented in this paper are not publicly available at this time but may be obtained from authors upon reasonable request.

Supplemental document. See Supplement 1 for supporting content.

References

1. E. H. K. Stelzer, "Light sheet fluorescence microscopy for quantitative biology," Nat. Methods **12**(1), 23–26 (2015).
2. O. E. Olarte, J. Andilla, E. J. Gualda, and P. Loza-Alvarez, "Light-sheet microscopy: a tutorial," Adv. Opt. Photonics **10**(1), 111 (2018).
3. B. C. Chen, W. R. Legant, K. Wang, L. Shao, D. E. Milkie, M. W. Davidson, C. Janetopoulos, X. S. Wu, J. A. Hammer, Z. Liu, B. P. English, Y. Mimori-Kiyosue, D. P. Romero, A. T. Ritter, J. Lippincott-Schwartz, L. Fritz-Laylin, R. D. Mullins, D. M. Mitchell, J. N. Bembenek, A. C. Reymann, R. Böhme, S. W. Grill, J. T. Wang, G. Seydoux, U. S. Tulu, D. P. Kiehart, and E. Betzig, "Lattice light-sheet microscopy: Imaging molecules to embryos at high spatiotemporal resolution," Science **346**(6208), 1257998 (2014).
4. F. Aguet, S. Upadhyayula, R. Gaudin, Y. Y. Chou, E. Cocucci, K. He, B. C. Chen, K. Mosaliganti, M. Pasham, W. Skillern, W. R. Legant, T. L. Liu, G. Findlay, E. Marino, G. Danuser, S. Megason, E. Betzig, and T. Kirchhausen, "Membrane dynamics of dividing cells imaged by lattice light-sheet microscopy," Mol. Biol. Cell **27**(22), 3418–3435 (2016).
5. N. Yamashita, M. Morita, W. R. Legant, B.-C. Chen, E. Betzig, H. Yokota, and Y. Mimori-Kiyosue, "Three-dimensional tracking of plus-tips by lattice light-sheet microscopy permits the quantification of microtubule growth trajectories within the mitotic apparatus," J. Biomed. Opt. **20**(10), 101206 (2015).
6. Z. Liu, W. R. Legant, B. Chen, L. Li, J. B. Grimm, L. D. Lavis, E. Betzig, and R. Tjian, "3D imaging of Sox2 enhancer clusters in embryonic stem cells," 1–29 (2014).
7. A. M. Valm, S. Cohen, W. R. Legant, J. Melunis, U. Hershberg, E. Wait, A. R. Cohen, M. W. Davidson, E. Betzig, and J. Lippincott-Schwartz, "Applying systems-level spectral imaging and analysis to reveal the organelle interactome," Nature **546**(7656), 162–167 (2017).
8. N. D. Condon, J. M. Heddleston, T. L. Chew, L. Luo, P. S. McPherson, M. S. Ioannou, L. Hodgson, J. L. Stow, and A. A. Wall, "Macropinosome formation by tent pole ruffling in macrophages," J. Cell Biol. **217**(11), 3873–3885 (2018).
9. A. T. Ritter, Y. Asano, J. C. Stinchcombe, N. M. G. Dieckmann, B. C. Chen, C. Gawden-Bone, S. van Engelenburg, W. Legant, L. Gao, M. W. Davidson, E. Betzig, J. Lippincott-Schwartz, and G. M. Griffiths, "Actin depletion initiates events leading to granule secretion at the immunological synapse," Immunity **42**(5), 864–876 (2015).
10. L. B. Crowe, P. F. Hughes, D. A. Alcorta, T. Osada, A. P. Smith, J. Totzke, D. R. Loiselle, I. D. Lutz, M. Gargesha, D. Roy, J. Roques, D. Darr, H. K. Lyerly, N. L. Spector, and T. A. J. Haystead, "A fluorescent Hsp90 probe demonstrates the unique association between extracellular Hsp90 and malignancy in vivo," ACS Chem. Biol. **12**(4), 1047–1055 (2017).
11. Y. Xiao, A. Faucherre, L. Pola-Morell, J. M. Heddleston, T.-L. Liu, T.-L. Chew, F. Sato, A. Sehara-Fujisawa, K. Kawakami, and H. Lopez-Schier, "High-resolution live imaging reveals axon-glia interactions during peripheral nerve injury and repair in zebrafish," Dis. Model. Mech. **8**(6), 553–564 (2015).
12. N. Trivedi, D. R. Stabley, B. Cain, D. Howell, C. Laumonnerie, J. S. Ramahi, J. Temirov, R. A. Kerekes, P. R. Gordon-Weeks, and D. J. Solecki, "Drebrin-mediated microtubule-actomyosin coupling steers cerebellar granule neuron nucleokinesis and migration pathway selection," Nat. Commun. **8**(1), 14484 (2017).
13. M. Ducros, A. Getz, M. Arizono, V. Pecoraro, M. Fernandez Monreal, M. Letellier, V. Nägerl, and D. Choquet, "Lattice light sheet microscopy and photo-stimulation in brain slices," SPIE BiOS **8**, 8 (2019).
14. A. M. Getz, M. Ducros, C. Breillat, A. Lampin-saint-amaux, S. Daburon, U. François, A. Nowacka, M. Fernández-monreal, E. Hosy, F. Lanore, H. L. Zieger, M. Sainlos, Y. Humeau, and D. Choquet, "High-resolution imaging and manipulation of endogenous AMPA receptor surface mobility during synaptic plasticity and learning," Sci. Adv. **8**(30), 5298 (2022).
15. M. Schwertner, M. J. Booth, M. A. A. Neil, and T. Wilson, "Measurement of specimen-induced aberrations of biological samples using phase stepping interferometry," J. Microsc. **213**(1), 11–19 (2004).
16. M. Schwertner, M. J. Booth, and T. Wilson, "Characterizing specimen induced aberrations for high NA adaptive optical microscopy," Opt. Express **12**(26), 6540 (2004).
17. M. J. Booth, "Adaptive optics in microscopy," Philos. Trans. R. Soc., A **365**(1861), 2829–2843 (2007).
18. N. Ji, "Adaptive optical fluorescence microscopy," Nat. Methods **14**(4), 374–380 (2017).
19. M. J. Booth, "Adaptive optical microscopy: The ongoing quest for a perfect image," Light: Sci. Appl. **3**(4), e165 (2014).
20. O. Azucena, J. Crest, J. Cao, W. Sullivan, P. Kner, D. Gavel, D. Dillon, S. Olivier, and J. Kubby, "Wavefront aberration measurements and corrections through thick tissue using fluorescent microsphere reference beacons," Opt. Express **18**(16), 17521 (2010).
21. R. Aviles-Espinosa, J. Andilla, R. Porcar-Guezenec, O. E. Olarte, M. Nieto, X. Levecq, D. Artigas, and P. Loza-Alvarez, "Measurement and correction of in vivo sample aberrations employing a nonlinear guide-star in two-photon excited fluorescence microscopy," Biomed. Opt. Express **2**(11), 3135 (2011).
22. A. Hubert, F. Harms, R. Juvénal, P. Treimany, X. Levecq, V. Loriette, G. Farkouh, F. Rouyer, and A. Fragola, "Adaptive optics light-sheet microscopy based on direct wavefront sensing without any guide star," Opt. Lett. **44**(10), 2514 (2019).

23. S. Imperato, F. Harms, A. Hubert, M. Mercier, L. Bourdieu, and A. Fragola, "Single-shot quantitative aberration and scattering length measurements in mouse brain tissues using an extended-source Shack-Hartmann wavefront sensor," Opt. Express **30**(9), 15250 (2022).

24. B. M. Hanser, M. G. L. Gustafsson, D. A. Agard, and J. W. Sedat, "Phase-retrieved pupil functions in wide-field fluorescence microscopy," J. Microsc. **216**(1), 32–48 (2004).

25. M. J. Booth, M. A. A. Neil, R. Juškaitis, and T. Wilson, "Adaptive aberration correction in a confocal microscope," Proc. Natl. Acad. Sci. U. S. A. **99**(9), 5788–5792 (2002).

26. A. Facomprez, E. Beaurepaire, and D. Débarre, "Accuracy of correction in modal sensorless adaptive optics," Opt. Express **20**(3), 2598 (2012).

27. D. Débarre, E. J. Botcherby, T. Watanabe, S. Srinivas, M. J. Booth, and T. Wilson, "Image-based adaptive optics for two-photon microscopy," Opt. Lett. **34**(16), 2495–2497 (2009).

28. J. Zeng, P. Mahou, M.-C. Schanne-Klein, E. Beaurepaire, and D. Débarre, "3D resolved mapping of optical aberrations in thick tissues," Biomed. Opt. Express **3**(8), 1898 (2012).

29. N. Olivier, D. Débarre, and E. Beaurepaire, "Dynamic aberration correction for multiharmonic microscopy," Opt. Lett. **34**(20), 3145–3147 (2009).

30. D. Debarre, M. J. Booth, and T. Wilson, "Image based adaptive optics through optimisation of low spatial frequencies," Opt. Express **15**(13), 8176 (2007).

31. M. E. Siemons, N. A. K. Hanemaaijer, M. H. P. Kole, and L. C. Kapitein, "Robust adaptive optics for localization microscopy deep in complex tissue," Nat. Commun. **12**(1), 3407 (2021).

32. D. Burke, B. Patton, F. Huang, J. Bewersdorf, and M. J. Booth, "Adaptive optics correction of specimen-induced aberrations in single-molecule switching microscopy," Optica **2**(2), 177 (2015).

33. L. Streich, J. C. Boffi, L. Wang, K. Alhalaseh, M. Barbieri, R. Rehm, S. Deivasigamani, C. T. Gross, A. Agarwal, and R. Prevedel, "High-resolution structural and functional deep brain imaging using adaptive optics three-photon microscopy," Nat. Methods **18**(10), 1253–1258 (2021).

34. M. J. Mlodzianoski, P. J. Cheng-Hathaway, S. M. Bemiller, T. J. McCray, S. Liu, D. A. Miller, B. T. Lamb, G. E. Landreth, and F. Huang, "Active PSF shaping and adaptive optics enable volumetric localization microscopy through brain sections," Nat. Methods **15**(8), 583–586 (2018).

35. L. Sherman, J. Y. Ye, O. Albert, and T. B. Norris, "Adaptive correction of depth-induced aberrations in multiphoton scanning microscopy using a deformable mirror," J. Microsc. **206**(1), 65–71 (2002).

36. K. F. Tehrani, J. Xu, Y. Zhang, P. Shen, and P. Kner, "Adaptive optics stochastic optical reconstruction microscopy (AO-STORM) using a genetic algorithm," Opt. Express **23**(10), 13677 (2015).

37. A. J. Wright, D. Burns, B. A. Patterson, S. P. Poland, G. J. Valentine, and J. M. Girkin, "Exploration of the optimisation algorithms used in the implementation of adaptive optics in confocal and multiphoton microscopy," Microsc. Res. Tech. **67**(1), 36–44 (2005).

38. N. Ji, D. E. Milkie, and E. Betzig, "Adaptive optics via pupil segmentation for high-resolution imaging in biological tissues," Nat. Methods **7**(2), 141–147 (2010).

39. R. Jorand, G. Le Corre, J. Andilla, A. Maandhui, C. Frongia, V. Lobjois, B. Ducommun, and C. Lorenzo, "Deep and clear optical imaging of thick inhomogeneous samples," PLoS One **7**(4), e35795 (2012).

40. A. Masson, P. Escande, C. Frongia, G. Clouvel, B. Ducommun, and C. Lorenzo, "High-resolution in-depth imaging of optically cleared thick samples using an adaptive SPIM," Nat. Publ. Gr. 1–14 (n.d.).

41. T. L. Liu, S. Upadhyayula, D. E. Milkie, V. Singh, K. Wang, I. A. Swinburne, K. R. Mosaliganti, Z. M. Collins, T. W. Hiscock, J. Shea, A. Q. Kohrman, T. N. Medwig, D. Dambournet, R. Forster, B. Cunniff, Y. Ruan, H. Yashiro, S. Scholpp, E. M. Meyerowitz, D. Hockemeyer, D. G. Drubin, B. L. Martin, D. Q. Matus, M. Koyama, S. G. Megason, T. Kirchhausen, and E. Betzig, "Observing the cell in its native state: Imaging subcellular dynamics in multicellular organisms," Science **360**(6386), eaaq1392 (2018).

42. J. Schöneberg, D. Dambournet, T. L. Liu, R. Forster, D. Hockemeyer, E. Betzig, and D. G. Drubin, "4D cell biology: big data image analytics and lattice light-sheet imaging reveal dynamics of clathrin-mediated endocytosis in stem cell–derived intestinal organoids," Mol. Biol. Cell **29**(24), 2959–2968 (2018).

43. V. Lakshminarayanan and A. Fleck, "Zernike polynomials: A guide," J. Mod. Opt. **58**(7), 545–561 (2011).

44. A. Maizel, D. Von Wangenheim, F. Federici, J. Haseloff, and E. H. K. Stelzer, "High-resolution live imaging of plant growth in near physiological bright conditions using light sheet fluorescence microscopy," Plant J. **68**(2), 377–385 (2011).

45. M. R. Rai, C. Li, and A. Greenbaum, "Quantitative analysis of illumination and detection corrections in adaptive light sheet fluorescence microscopy," Biomed. Opt. Express **13**(5), 2960 (2022).

46. L. A. Royer, W. C. Lemon, R. K. Chhetri, Y. Wan, M. Coleman, E. W. Myers, and P. J. Keller, "Adaptive light-sheet microscopy for long-term, high-resolution imaging in living organisms," Nat. Biotechnol. **34**(12), 1267–1278 (2016).

47. L. A. Royer, W. C. Lemon, R. K. Chhetri, and P. J. Keller, "A practical guide to adaptive light-sheet microscopy," Nat. Protoc. **13**(11), 2462–2500 (2018).

48. W. R. Legant, L. Shao, J. B. Grimm, T. A. Brown, D. E. Milkie, B. B. Avants, L. D. Lavis, and E. Betzig, "High-density three-dimensional localization microscopy across large volumes," Nat. Methods **13**(4), 359–365 (2016).

49. I. Izeddin, M. El Beheiry, J. Andilla, D. Ciepielewski, X. Darzacq, and M. Dahan, "PSF shaping using adaptive optics for three-dimensional single-molecule super-resolution imaging and tracking," Opt. Express **20**(5), 4957 (2012).